Characterization of viscoelastic damping mechanism in a delaminated structure

Mechanical Systems and Signal Processing 219 (2024) 111600

Contents lists available at ScienceDirect

Mechanical Systems and Signal Processing

journal homepage: www.elsevier.com/locate/ymssp

Characterization of viscoelastic damping mechanism in a delaminated structure

Sh. Kiasat [a,b,*], A.S. Nobari [a,c,1], M. Filippi [b,2], E. Carrera [b,3]

[a] Faculty of Aerospace Engineering, Amirkabir University of Technology, 159163-4311, Tehran, Iran
[b] Mul2 Group, Department of Mechanical and Aerospace Engineering, Politecnico di Torino, 10129, Torino, Italy
[c] Aeronautics Engineering Department, Imperial College, London, United kingdom

ARTICLE INFO

Communicated by S. Fassois

Keywords:
Delamination
Viscoelasticity
Damping mechanisms
Carrera unified formulation
Prony's series
SHM

ABSTRACT

This work aims to examine modal damping behavior in a delaminated viscoelastic structure. A numerical assessment of a viscoelastic delaminated structure using one-dimensional theories based on the Carrera Unified Formulation (CUF) was conducted to achieve this goal. The CUF-based models were formulated with Lagrange polynomials and a layer-wise approach, which made it possible to simulate inter-layer defects with relative ease, computational efficiency, and accuracy similar to 3D models. The current framework is based on time-domain method verification and exploits the frequency-based structural damping model to estimate the modal loss factor and natural damped frequency. The numerical outcomes confirm the approximation of the viscoelastic damping by the structural damping model and validate the adopted numerical method for solving the complex frequency-dependent eigenvalue problem with a comparison of the literature. In conclusion, by evaluating the modal parameters, this research provides an innovative, comprehensive understanding of the viscoelastic damping mechanism in a delaminated structure. The proposed numerical method based on the CUF can be used to simulate inter-layer defects and determine the damping behavior of viscoelastic structures, which can have significant implications for structural health monitoring and maintenance.

1. Introduction

Damage detection is a critical aspect of designing load-sensitive structures in industries (e.g., transportation and aerospace) where a reliable safety method of safety assessment is vital, and the consequences of structural failure can be severe. The goal of damage detection is to recognize the presence of damage, determine its location, and estimate its extent. By doing so, more efficient structures can be designed, and the service life of load-sensitive systems can be evaluated and improved. In recent decades, many numerical and experimental efforts have been made for damage identification purposes in the structures [1–6]. In the frequency domain data, the deficiency damage in the structure can be identified by observing modal parameter alterations, including natural frequency [7,8], mode shape curvature [9,10], and modal damping [11,12]. Previous research has observed that despite its global nature, the natural frequency is generally insensitive to (minor) damages [6]. Also, the locality of the mode shape curvature makes it unlikely to be used

* Corresponding author at: Mul2 Group, Department of Mechanical and Aerospace Engineering, Politecnico di Torino, 10129, Torino, Italy.
E-mail addresses: shabnam.kiasat@polito.it (Sh. Kiasat), a.salehzadeh-nobari@imperial.ac.uk (A.S. Nobari), matteo.filippi@polito.it (M. Filippi), erasmo.carrera@polito.it (E. Carrera).
[1] Professor of Aerospace Structures.
[2] Assistant professor.
[3] Professor of Aerospace Structures and Aeroelasticity.

https://doi.org/10.1016/j.ymssp.2024.111600
Received 13 October 2023; Received in revised form 15 April 2024; Accepted 2 June 2024
Available online 10 June 2024

for detecting defects in the arbitrary locations of the structures. The research's primary motivation is to investigate the potential of modal damping as a damage index (DI) for detecting interlaminar delamination in laminate structures. The authors' previous experimental research [6] demonstrated significant variations in modal damping with the extent of delamination in a composite structure. However, the researchers observed that the modal damping variations did not follow a specific pattern with the size variation of interlaminar delamination in their experimental background. They attributed this inconsistency to different damping mechanisms in delaminated composite structures, such as viscoelasticity, friction, hysteresis, and others [13,14]. They concluded that one of these mechanisms likely dominates each vibration mode of the composite structure. To better understand the individual contributions of different damping mechanisms and their impact on modal loss factor variations, the researchers aimed to provide a numerical model for characterizing modal damping. They recognized the complexity of numerical modeling for damping, as it is an extremely sensitive dynamic parameter. Therefore, this study focused on the numerical simulation of the viscoelastic (VE) damping mechanism. By simulating VE damping, they aimed to explore its role and behavior concerning interlaminar delamination. It is worth noting that few related studies have utilized modal damping as a damage index, as mentioned in [15]. Therefore, providing a numerical model to specify the measured modal damping would benefit further research and application of damping-based damage detection techniques.

Laminated structures may experience various damage modes due to initial geometric imperfections [16], mechanical properties, boundary conditions, and applied loadings [17]. Failure mechanisms can be categorized based on the defect location, into intralaminar [18] and interlaminar [19]. Intralaminar damage can be seen at the free edges of the structure and occurs typically due to the extreme stresses on free edges. Interlaminar damage arises in the middle parts of the structure due to geometric defects during manufacturing or impact loads. One of the most common forms of interlaminar damage is interlaminar delamination (from now on, it is called delamination) [20], which means that large areas or multiple numbers may lead to catastrophic failure of the structure. It is thus vital to detect the occurrence, location, and severity.

From the structural health monitoring (SHM) point of view, the presence of delamination leads to fluctuation in the load-bearing threshold of the structure [21]; therefore, identifying the existence and position of delamination can be very helpful in estimating the structure's service life. Except for oscillation-based techniques, none of the current Non-Destructive Technique (NDT)-based methods can be applied in real-time, online manner. Applying techniques like Ultrasound or Acoustic Emission requires out-of-service, off-line measurements.

On the other hand, oscillation-based techniques, such as Lamb waves and/or vibration-based techniques, can detect damage in real-time. The vibration-based SHM techniques (VHM) are logistically relatively simple and low-cost. However, VHM techniques generally suffer from insensitivity to minor damages [22], valid except for modal damping, which is both a global characteristic of the structure and sensitive to small damages (delamination) [6]. Due to the non-classical effects of delamination, a numerical method that can accurately estimate displacement, strain, and stress while incorporating local and nonlinear effects is needed. However, traditional 3D solid elements are not time-effective for this application. Researchers have proposed various models in the literature to simulate the dynamic response of delaminated composite plates without resorting to computationally expensive solid elements. These alternative models aim to capture the intricate behavior of delamination while mitigating computational costs. They often utilize simplified approaches such as interface elements, which directly represent the delamination interface. This enables efficient modeling of the interaction between adjacent layers, achieving accuracy without the computational burden of solid elements. Cohesive Zone Models ($CZMs$) [23] describe the fracture process at the delamination interface, employing cohesive laws to govern the separation behavior between layers and striking a balance between accuracy and computational efficiency. Additionally, mixed-mode fracture criteria [24] assess the mode mix at the delamination front, enhancing accuracy by considering different fracture modes while being computationally more efficient than full solid element simulations. In this research, higher-order 1D models based on the Carrera Unified Formulation (CUF) are used to address this issue [25–28]. The power suit of using CUF is that the arbitrary variable in the expansion function allows for a proper structural theory to be adapted to consider the nonlinear and non-classical effects resulting from separation in the structure [29]. This paper explores how delamination impacts a laminate structure's modal parameters, especially the modal loss factor. In ideal conditions for a pristine composite plate, the matrix's VE effects are the main damping source. However, when delaminated, the VE contribution can change, and other damping mechanisms caused by interface contact can get involved. Although the layered structure considered is not a typical composite, it helps separate the different damping mechanisms involved in delaminated composite and assess their significance on a modal basis. Therefore, this study serves two purposes: 1- studying the changes and trends in VE-induced damping due to delamination without considering the effect of other damping mechanisms. 2- Assessing the performance and validity of modal damping calculations for the layered VE structures when only measurement data are available. Section 2 is dedicated to presenting a theoretical review of the structural model used in the study. Section 3 is focused on an assessment of the adopted validation method. Section 4 presents and interprets the numerical results obtained from the simulation. Finally, Section 5 provides the conclusions of the study.

2. Layer-wise high-fidelity finite beam elements

The unified formulation states that the displacement field ($\vec{u}(x, y, z)$) can be expressed as a series of generic cross-sectional functions (F_τ) in the x–z plane and for a beam-like structure, *generalized* displacement vectors ($\vec{u}_\tau$) along the y-axis. The generic cross-sectional functions are chosen a priori based on the structure's geometry, while the generalized displacement vectors are interpolated using a classic finite element method (FEM). Eq. (1) shows the 3D displacement vector of a beam as a product between

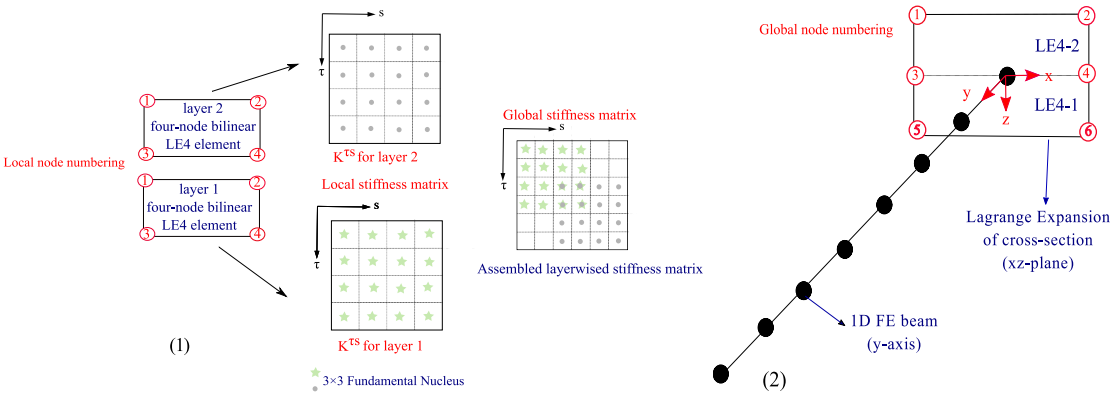

Fig. 1. (1) Assembly process of the local stiffness matrices in a two-layer laminated beam with LW theory. (2) FE discretization of 1D beam through CUF.

the generic cross-sectional functions (F_τ) and the *generalized* displacement vectors ($\vec{u}_\tau$) along the beam axis (y-axis) where the repeated subscript τ indicates summation.

$$\vec{u}(x,y,z) = F_\tau(x,z)\vec{u}_\tau(y), \qquad \tau = 1,2,\dots,M \tag{1}$$

Taylor-like (TE) and Lagrange expansion (LE) functions are two common choices of expansion functions that are essential factors in the accuracy of the CUF model. The LE models are particularly suitable for a layer-wise (LW) description of multi-layered structures [28] since they are equipped with pure displacement variables and layer-dependent unknowns. If the LE approach is adopted, the cross-section is divided into sub-domains that can coincide with the physical layers. For each sub-domain, one or more Lagrange-type elements can be used. The degree of polynomial expansion of each element depends on the type of Lagrange expansion used. For example, three-node linear (LE3), four-node bilinear (LE4), nine-node quadratic (LE9), and sixteen-node bi-cubic (LE16) polynomials can be used to formulate various beam theories. Fig. 1(1) shows the representation of the stiffness matrix assembly for the 2-layer cross-section, while Fig. 1(2) shows the two Lagrange-type elements (LE4) used in the cross-section. For the sake of brevity, the details of the LE elements, the interpolation functions of Lagrange 1D models, and the displacement fields are not mentioned. Interested readers are referred to the book by Carrera et al. [30].

The classical FEM is adopted here to discretize the beam along the length (y-axis) due to its ease of use for various geometries and boundary conditions (BCs). The displacement vector is given by Eq. (2)

$$\vec{u}_\tau(y) = N_i(y)\vec{q}_{\tau i} \qquad i = 1,2,\dots,p+1 \tag{2}$$

where in Eq. (2), $N_i(y)$ is the ith shape function, $\vec{q}_{\tau i}$ is the vector of nodal unknowns (defined by Eq. (3)) associated with the ith shape function, and the summation over i ranges from 1 to $p+1$, where p is the order of the shape functions. The FE discretization of a two-layer beam through CUF and expanded cross-section by LE4 is represented in Fig. 1(2).

$$\vec{q}_{\tau i} = \left\{ \begin{array}{ccc} q_{x_{\tau i}} & q_{y_{\tau i}} & q_{z_{\tau i}} \end{array} \right\}^{\mathrm{T}} \tag{3}$$

It is worth noting that in a CUF-based FE model, the choice of cross-section polynomials is independent of the beam FE along the y-axis. The shape functions N_i used in the beam FE approach can be found in many FEM references, such as Ref. [31]. This work will adopt the classical 1D four-node cubic elements for the shape function along the y-axis, which is common in structural mechanics and provides a good balance between accuracy and computational efficiency. The principle of virtual displacements (PDVs) is a powerful tool for analyzing the behavior of complex systems, particularly in the context of FE analysis. It is adopted to drive the equations of motion ($EOMs$), see Eq. (4)

$$\delta L_{\mathrm{int}} = \delta L_{ext} + \delta L_{ine} \tag{4}$$

In Eq. (4), L_{int} and L_{ine} indicate the strain and inertial energies, respectively, δ stands for virtual variation. Assuming the work of external loadings L_{ext} is zero Eq. (4) becomes Eq. (5)

$$\delta L_{ine} - \delta L_{\mathrm{int}} = \int_V (\delta u^T \rho \ddot{u}) dV - \int_V (\varepsilon_p^T \sigma_p + \varepsilon_n^T \sigma_n) = 0 \tag{5}$$

In Eq. (5) u and $\ddot{u}$ are the displacement and acceleration vectors, respectively, and ρ is the material density. The stresses (σ) and strains (ε) are defined as Eq. (6)

$$\begin{array}{ll} \varepsilon_p = \left\{ \begin{array}{ccc} \varepsilon_{zz} & \varepsilon_{xx} & \varepsilon_{xz} \end{array} \right\}^T & \sigma_p = \left\{ \begin{array}{ccc} \sigma_{zz} & \sigma_{xx} & \sigma_{xz} \end{array} \right\}^T \\ \varepsilon_n = \left\{ \begin{array}{ccc} \varepsilon_{zy} & \varepsilon_{xy} & \varepsilon_{yy} \end{array} \right\}^T & \sigma_n = \left\{ \begin{array}{ccc} \sigma_{zy} & \sigma_{xy} & \sigma_{yy} \end{array} \right\}^T \end{array} \tag{6}$$

In Eq. (6), the subscripts p and n correspond to the terms on the cross-section and the orthogonal plane to the cross-section, respectively. Eqs. (7)–(8) describe the linear relations between strain–displacement and stress–strain (Hooke's law) for an isotropic material.

$$\begin{aligned}\varepsilon_p &= D_p u \\ \varepsilon_n &= (D_{ny} + D_{np})u\end{aligned} \tag{7}$$

$$\begin{aligned}\sigma_p &= \tilde{C}_{pp}\varepsilon_p + \tilde{C}_{pn}\varepsilon_n \\ \sigma_n &= \tilde{C}_{np}\varepsilon_p + \tilde{C}_{nn}\varepsilon_n\end{aligned} \tag{8}$$

where D_p, D_{ny}, and D_{np} are differential linear operators [30]. The explicit forms of the terms of $\left[\tilde{C}\right]$ are found in Ref. [32]. The virtual variation of strain energy using Eqs. (1), (2), (7), and (8) is written as Eq. (9)

$$\delta L_{\text{int}} = \delta q_{\tau i}{}^{T} K^{ij\tau s} q_{si} \tag{9}$$

where $K^{ij\tau s}$ is the complex fundamental nucleus of the stiffness matrix defined like Eq. (10).

$$\begin{aligned}K^{ij\tau s} &= I_l^{ij} \lhd (D_{np}^T F_\tau I)[\tilde{C}_{np}^k (D_p F_s I) + \tilde{C}_{nn}^k (D_{np} F_s I)] \\ &+ (D_p^T F_\tau I)[\tilde{C}_{pp}^k (D_p F_s I) + \tilde{C}_{np}^k (D_{np} F_s I)] \rhd \Omega \\ &+ I_l^{ij,y} \lhd [(D_{np}^T F_\tau I)\tilde{C}_{nn}^k + (D_p^T F_\tau I)\tilde{C}_{pn}^k] F_s \rhd \Omega I_{\Omega y} \\ &+ I_l^{i,jy} I_{\Omega y} \lhd F_\tau \left[\tilde{C}_{np}^k (D_p F_s I) + \tilde{C}_{nn}^k (D_{np} F_s I)\right] \rhd \Omega \\ &+ I_l^{i,j,y} I_{\Omega y} \lhd F_\tau \tilde{C}_{nn}^k F_s \rhd \Omega I_{\Omega y}\end{aligned} \tag{10}$$

where

$$I_{\Omega y} = \begin{bmatrix} 0 & 0 & 1 \\ 1 & 0 & 0 \\ 0 & 1 & 0 \end{bmatrix} \lhd \ldots \rhd \Omega = \int_\Omega \ldots d\Omega \tag{11}$$

$$\left(I_l^{ij}, I_l^{ij,y}, I_l^{i,jy}, I_l^{i,y,j,y}\right) = \int_l \left(N_i N_j, N_i N_{j,y}, N_{i,y} N_j, N_{i,y} N_{j,y}\right) dy \tag{12}$$

The virtual variation of inertia energies is represented as Eq. (13),

$$\begin{aligned}\delta L_{ine} &= \int_l \delta q_{\tau i}^T M^{ij\tau s} \ddot{q}_{sj} dy \\ &= \int_l \delta q_{\tau i}^T N_i \left[\int_\Omega \varphi^k \left(F_\tau I\right)\left(F_s I\right) d\Omega\right] N_j \ddot{q}_{sj} dy\end{aligned} \tag{13}$$

The fundamental mass matrix ($M^{ij\tau s}$) components that have real values are as Eq. (14).

$$\begin{aligned}M_{xx}{}^{ij\tau s} &= M_{yy}{}^{ij\tau s} = M_{zz}{}^{ij\tau s} = I_l^{ij} \lhd \left(F_\tau \varphi^k I F_s\right) \rhd \\ M_{xy}{}^{ij\tau s} &= M_{xz}{}^{ij\tau s} = M_{yx}{}^{ij\tau s} = M_{yz}{}^{ij\tau s} = M_{zx}{}^{ij\tau s} = M_{zy}{}^{ij\tau s} = 0\end{aligned} \tag{14}$$

In the homogeneous $EOMs$ (Eq. (15)), complex eigenvalues $\Lambda_n^* = \Lambda_n + i\Lambda_n'$ and their corresponding complex eigenvectors are found by assuming a periodic solution $q = \bar{q}e^{i\omega^* t}$. For each mode, the damped natural frequency is given by $\omega_n = \sqrt{\Lambda_n}$, and the corresponding modal loss factor is defined as $\eta_n = \frac{\Lambda'_n}{\Lambda_n}$.

$$\left(-\Lambda_n^* M + K\left(\omega_n\right)\right)\bar{q}_n = 0 \tag{15}$$

In solving the eigenvalue problem in Eq. (15), classical eigenvalue methods are unsuitable when the stiffness matrix is dependent on frequency. Other methods, such as the complex eigenvalue method [33], strain energy method [34], and direct frequency response method [35], have limitations in their applicability or accuracy. Therefore, numerical methods such as Arnoldi's method [36], order reduction [37], and iterative algorithms [38] have been developed to approximate the response of parametric complex eigenvalue problems. In this research, the numerical model has been verified based on the Approached Complex Eigenmodes (ACM) [39] and the Iterative Complex Eigenmodes Method (ICM) [40] and compared with the Exact Complex Eigenmodes method (ECM) [39]. Here is a brief description of the ACM and ICM that the numerical model of this research has been verified based on.

Analysis around the delayed real frequency (ACM)

In this method, the effect of frequency dependency is considered by estimating the stiffness matrix $[K(\omega)]$ around the natural frequency corresponding to the delayed elasticity condition, denoted by ω_0, See (16) where $[K]$ and $[M]$ are stiffness and mass matrices, respectively.

$$\left([K(\omega_0)] - \omega^2[M]\right)\{U\} = 0 \tag{16}$$

The solution of Eq. (16) yields the complex natural frequencies ω_n and the corresponding complex eigenmodes $\{U_n\}$.

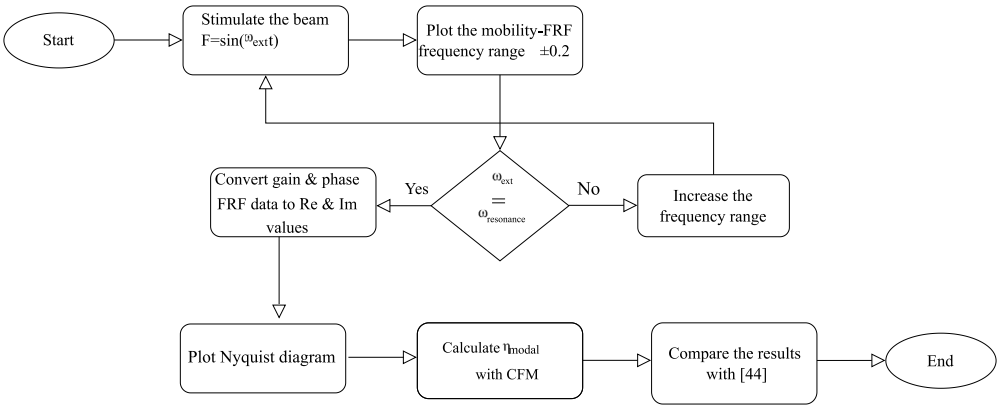

Fig. 2. Time-domain analysis steps.

Iterative complex eigenvalue method (ICM)

The solution of Eq. (17) starts at a constant frequency. Then, the eigenvalue problem is solved iteratively and updated for each frequency individually until the desired frequency range is covered.

$$\left(\left[K^*(\omega)\right] - \omega^{*^2}\left[M\right]\right)\left\{U^*\right\} = 0 \tag{17}$$

In Eq. (17), the complex stiffness matrix ($K^*(\omega)$) is comprised of the real and imaginary parts ($K'(\omega)$ and $K''(\omega)$, respectively), and the eigenfrequency ω^* is a complex value with a real part (ω') and an imaginary part (ω''). The eigenfrequency's real part represents the system's damped natural frequency, while the imaginary part represents the decay rate of the dynamic process. Eq. (17) can be transformed into a nonlinear generalized eigenvalue problem by defining a complex eigenvalue $\lambda^* = \omega^{*^2}$, and this leads to Eq. (18).

$$K^*(\omega)\,U^* = \lambda^* M U^* \tag{18}$$

The iterative process ends when the condition in Eq. (19) is established.

$$\frac{\left\|\omega_{j+1} - \omega_j\right\|}{\omega_j} \le \varepsilon \tag{19}$$

where ω_j and ω_{j+1} are the eigenfrequencies obtained in the current and previous iterations, respectively, and ε is a small tolerance value that determines the desired accuracy of the solution. In each frequency step, the storage modulus and loss factor are determined using the frequency in the previous step ω_j, and the complex eigenfrequency ω_{j+1} is obtained by solving the nonlinear generalized eigenvalue problem in Eq. (18).

3. Verification of damping identification method

The dynamic properties of VE structures are inherently time-dependent due to the time-dependent nature of VE properties, such as creep compliance and relaxation modulus [41]. This can lead to complexity in modeling viscous damping in the time domain. Therefore, a common approach is to transform the $EOMs$ to the frequency domain [42], apply the structural damping (loss factor) model in the frequency domain, and solve the frequency-dependent eigenvalue problem to find the resonance frequencies and modal loss factors. In this respect, ACM and ICM methods are used. The described VE structure eigen solution methods suffer from 2 difficulties, namely, 1. It is tough to apply it to nonlinear problems when contact (and friction) gets involved in delamination modeling, and 2. It is does not apply to experimentally measured data, and a means of Experimental Modal Analysis (EMA) is required. As the most accurate EMA method of identification of the modal damping, the Circle Fit Method (CFM) can be used.

This section aims to verify the modal loss factors of the VE laminate structures calculated by ACM and ICM methods with those identified by the CFM. To simulate the measured data for Circle Fit (CF) analysis, $FRFs$ of the laminate structure are computed through a step-sine time history analysis (see Fig. 2). A frequency-dependent shear modulus based on Prony's series coefficients is used to model the VE part of the structure. The Prony's series coefficients are obtained using frequency-domain dynamic data, and data curve-fitting is performed for analytical [43] and numerical data. The authors then use this model to reproduce the results of their previous research [44] in the time domain with acceptable accuracy to confirm the efficiency of the frequency-domain methods (ACM and ICM).

Anelastic Displacement Fields model

Consider a sandwich beam that consists of elastic faces and a VE core. The core is homogeneous, linear, and isotropic, which its characteristics vary with frequency. The Anelastic Displacement Field (ADF) model is based on the decomposition of strains into the elastic part, which is proportional to the stress, and the inelastic part, which corresponds to different relaxation processes [45]. The nodal displacement of DOFs is considered as Eq. (20), where q^e and q_i^a indicate the nodal displacement vectors of the elastic

Table 1
Maxwell parameters of $3MISD112$ VE material at 20 °C [43] and correspondence extracted Prony's series parameters by the present work.

i	Δ_i [a] [43]	Ω_i [b] [43]	g_i [c]	τ_i [d]
	$G_0 = 0.0511$ (Mpa)		$g_\infty = 0.016$	
1	2.8164	31.1176	0.83169	1.65157e−2
2	13.1162	446.4542	−0.82754	1.50946e−2
3	45.4655	5502.5318	0.97985	9.94618e−4

[a] Material parameter.
[b] Material parameter.
[c] Present work.
[d] Present work.

and VE parts, respectively [46], and i is Prony series index. By including the strain in the strain energy of the VE material in the FEM, the ADF model can capture the time-dependent behavior of VE structures.

$$q^e = q - \sum_i q_i^a \tag{20}$$

Using Eq. (20) results in the governing EOMs as Eq. (21) where $K_c^\infty = (1 + \sum_i \Delta_i)K_c^0$ that Δ_i represents correspondent relaxation resistance, K_c^0 is the elastic stiffness of the VE core, and K_p is the stiffness matrix of the elastic faces.

$$M\ddot{q} + D\dot{q} + (K_c^\infty + K_p)q - K_c^\infty \sum_i q_i^a = F \tag{21}$$

Thus, the ADF model is further defined by Eq. (22) which presents a relation where $DOFs$ associated with inelastic displacements are expressed.

$$\frac{C_i}{\Omega_i} K_c^\infty q_i^a - K_c^\infty q + C_i K_c^\infty q_i^q = 0 \tag{22}$$

where $C_i = \frac{1+\sum_i \Delta_i}{\Delta_i}$ and Ω_i are Maxwell parameters that are interpolated by master curve fitting of experimental values of $G(\omega)$. Ω_i is the inverse of the characteristic relaxation time at constant strain. Therefore, the VE law is defined as Eq. (23).

$$G(\omega) = G_0 \left(1 + \sum_{i=1}^{n} \frac{\Delta_i \omega}{\omega - j\Omega_i} \right) \tag{23}$$

where in Eq. (23), G_0 is the delayed elasticity of shear modulus, and $j = \sqrt{-1}$. The loss factor (η) equals the ratio of the imaginary part to the real part of Eq. (23). It is worth noting that $\eta(0) = \eta(\infty) = 0$ means that the energy dissipation occurs only in the transition zone. At the lower and upper bound of ω, the shear modulus tends to its static (relaxed) and instantaneous (unrelaxed) values, i.e., $\lim G(\omega)_{\omega \to 0} = G_0$ and $\lim G(\omega)_{\omega \to \infty} = G_\infty$. The ADF parameters of $3MISD112$ are displayed in Table 1 [43].

Extraction of the Prony series coefficients from dynamic frequency data

Eq. (24) shows the expression for the Prony series, where $g(t)$ is the relaxation function, g_i is the amplitude of the ith exponential function, τ_i is the relaxation time associated with the ith exponential function, and N is the number of exponential functions in the series. The Prony series can be used to model the time-dependent behavior of VE materials in the linear regime, which is generally valid in the range of small strains.

$$g(t) = 1 - \sum_{i=1}^{N} g_i (1 - e^{-\frac{t}{\tau_i}}) \tag{24}$$

If dynamic frequency data is available for a VE material, the Prony series coefficients can be determined using curve-fitting techniques and Eq. (25). One common approach is to use the least-squares method to minimize the difference between the frequency-dependent shear modulus and the Prony series. The process typically involves the following steps: 1. Take an initial guess for the Prony series coefficients, including the relaxation times τ_i and the amplitudes g_i. 2. Calculate the storage shear modulus $G'(\omega)$ and the loss modulus $G''(\omega)$ using the Prony series coefficients, a value for N, and the initial guess for τ_i and g_i. 3. Compute the difference between the calculated $G'(\omega)$ and $G''(\omega)$ and the experimental frequency data [43]. 4. Use an optimization algorithm, such as a nonlinear least-squares algorithm, to minimize the residual between the calculated values and the frequency data by adjusting the Prony series coefficients. 5. Repeat steps 2–4 with different initial guesses for the Prony series coefficients until a satisfactory fit is achieved. Table 1 shows an example of the Prony series coefficients that the authors extracted from dynamic frequency data using the method described.

$$\begin{aligned} G'(\omega) &= G_0[(1 - \textstyle\sum_{i=1}^{N} g_i) + (\sum_{i=1}^{N} \frac{g_i {\tau_i}^2 \omega^2}{1+{\tau_i}^2\omega^2})] \\ G''(\omega) &= G_0 \textstyle\sum_{i=1}^{N} \frac{g_i {\tau_i}^2 \omega^2}{1+{\tau_i}^2\omega^2} \end{aligned} \tag{25}$$

Table 2
Comparison of natural frequency (Hz) of frequency-domain models with resonance frequency of time-domain analysis.

	ω_1	ω_2	ω_3	ω_4	ω_5
ECM[a] [39]	63	316.5	823.29	1530.6	–
ICM[b] [44]	64.99	323.16	840.87	1546.76	1024.84[c]
FRM[d]	61	315	804.9	1527.4	1063

[a] Exact complex eigenmodes.
[b] Iterative complex eigenmodes.
[c] Torsion mode.
[d] Frequency response method, present work.

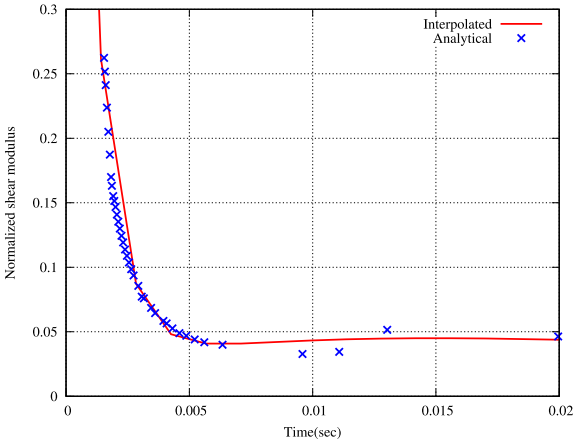

Fig. 3. Data evaluation of 3MISD112 VE material at 20 °C.

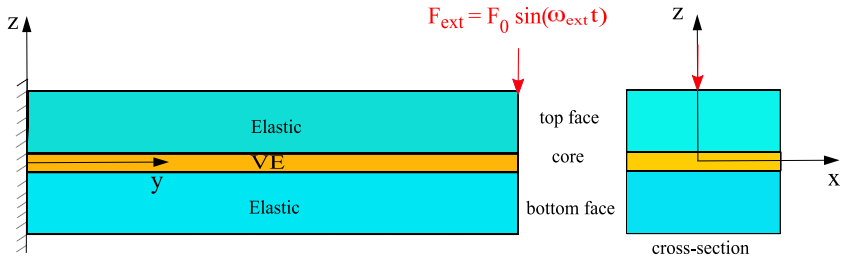

Fig. 4. Schematic of sandwich beam, location and type of loading for extracted point-FRFs in Fig. 5.

Data curve fitting of 3M ISD11 VE material

Fig. 3 depicts the curve fitting of the dynamic data and extracted the parameters of the Prony series, where g_∞ is the long-term normalized shear modulus.

Time-domain analysis using frequency-domain data

As shown in Fig. 4, the case study is a cantilevered thin VE layer bounded between stiffening elements, which are elastic metal with Young's modulus $E_f = 69$ (GPa), density $\rho_f = 2766$ (kgm^{-3}), and Poisson's ratio $\nu_f = 0.3$. The $3MISD112$ VE middle core with the thickness $h_c = 0.127$ (mm), density, and Poisson's ratio $\rho = 1600$ (kgm^{-3}) and $\nu = 0.49$, respectively [43,47] is considered (see Fig. 4). The length and width of the beam have been assumed to be equal to $L = 177.8$ (mm) and $b = 12.7$ (mm), respectively. Filippi and Carrera extracted the damped natural frequencies and the modal loss factors corresponding to the first four bending modes of the structure in Fig. 4 by the structural damping model [44] using ICM. They conducted a convergence study with the literature where the results obtained from Exact Complex Eigenmodes ($ECMs$) techniques [39]. In this research, We performed a time-domain analysis to confirm the accuracy of the previous work results [44] as well as the applicability of the CFM to VE structures. See the flowchart in Fig. 2.

Fig. 5 shows mobility-frequency Response Function (FRF) plots of each mode, and Table 2 indicates a good match between Resonance frequencies of time-domain analysis and natural frequencies of frequency-domain models.

The Circle Fit Method (CFM) was first introduced by Kennedy and Pancu [48] and is mainly developed with a structural damping model in mind; here, we will look at its applicability to VE damping. The CFM extracts the modal loss factor from the Nyquist plot of the frequency response function (FRF) of a single degree of freedom ($SDOF$) system. The Nyquist plot of the FRF is circle-like

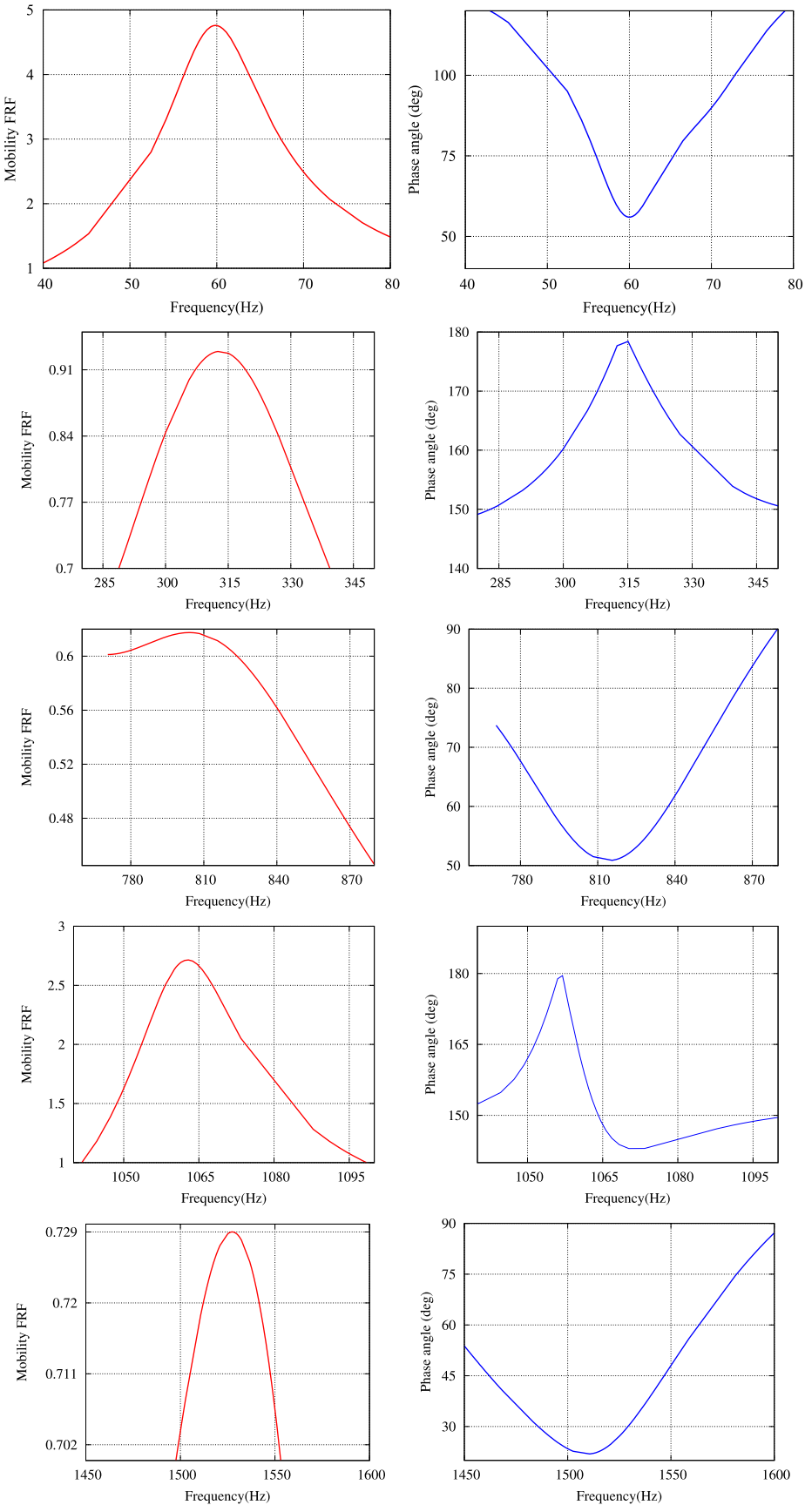

Fig. 5. Mobility-FRF and corresponding phase angle of five modes of the beam for the beam with BC and loading in Fig. 4 at (0,l,t/2).

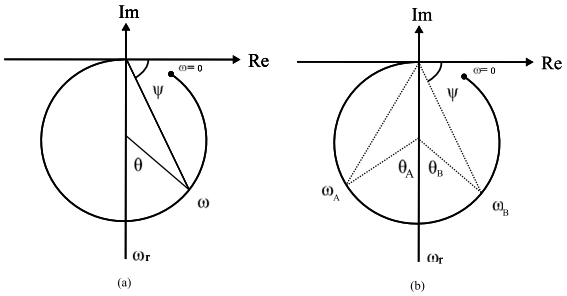

Fig. 6. Modal circle properties.

Table 3
Comparison of modal loss factors of frequency-domain models with modal damping of time-domain analysis.

	η_1	η_2	η_3	η_4	η_5
ECM[a] [39]	0.196	0.187	0.160	0.0948	–
ICM[b] [44]	0.22	0.199	0.156	0.0864	0.021
CFM[c]	0.194	0.186	0.11	0.10	0.023

[a] Exact complex eigenmodes.
[b] Iterative complex eigenmodes.
[c] Circle-fit method, present work.

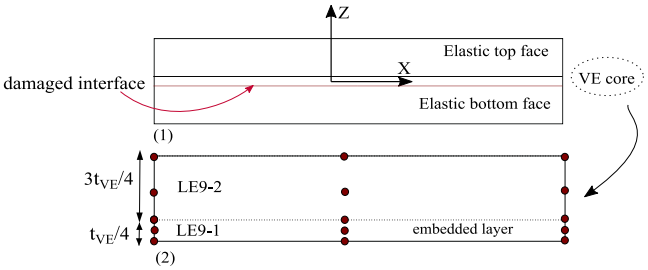

Fig. 7. (1) Cross-section view of through-the-length delamination. (2) Mesh refinement details in VE core.

arcs near the natural frequency, and if the damping model parameters are appropriately set, the Nyquist plot is an exact circle. The modal loss factor can be extracted from the geometric relations of the circle-like arcs in the Nyquist plot, as shown in Fig. 6 with Eqs. (26)–(27)

$$\eta = \frac{(\omega_A^2 - \omega_B^2)}{4\omega_r(\omega_A \tan(\theta_A/2) + \omega_B \tan(\theta_B/2))} \tag{26}$$

For lightly-damped systems,

$$\eta = \frac{(\omega_A - \omega_B)}{2\omega_r(\omega_A \tan(\theta_A/2) + \omega_B \tan(\theta_B/2))} \tag{27}$$

For multi-degree of freedom ($MDOF$) systems, the Nyquist plots of the FRF approach circle-like arcs near resonances. The factors that cause the Nyquist diagram to deviate from a circular form are the interference of the modes or nonlinear effects. If the underlying damping mechanism is deemed viscous, mobility-FRF data must be used to fit the circle. The Nyquist diagram rotates 90° on the Argand plane relative to where receptance-FRF data was used for a system with a structural damping model. An $MDOF$ system can be considered a collection of separated $SDOF$ systems in the resonance neighborhood in which the effect of other modes in the FRF is negligible or the contribution of the out-of-range modes to the total frequency response is constant. This complex constant does not affect the circular form of the Nyquist diagram and merely maps the center of the circle. Interested readers are referred to [48] for a comprehensive study of the CFM. Table 3 compares the modal damping values obtained using different techniques.

The results show that the modal damping values obtained using the CFM in the present work are comparable to those obtained using the ICM and ECM. The CFM method extracted the modal damping values for all modes, including the higher modes, which is important for accurately modeling of the structure's dynamic behavior.

After the assessment of ICM and ECM, a summary of the findings of this section for the CUF-based FE model of Fig. 4 can be observed in Table 4.

Table 4
Natural damped frequencies (Hz) and modal loss factors for the structure Fig. 4 and viscoelastic law Eq. (23).

	ω_1	ω_2	ω_3	ω_4	ω_5	η_1	η_2	η_3	η_4	η_5
20 °C										
ECM[a] [39]	63.07	316.54	823.29	1530.60	–	0.196	0.187	0.160	0.0948	–
ICM[b] [44]	65.001	323.228	841.071	1547.264	1042.197	0.220	0.199	0.156	0.0863	0.0205
CUF-LE9[c]	63.2	319.8	827.32	1541.5	1040.15	0.270	0.20	0.172	0.095	0.0210
27 °C										
ECM [39]	65.34	326.08	849.49	1567.53	–	0.156	0.255	0.278	0.269	–
ICM [44]	65.80	330.81	866.11	1595.99	1042.47	0.158	0.261	0.284	0.272	0.0469
CUF-LE9	64.31	322.40	833.83	1586.72	1042.99	0.144	0.272	0.30	0.291	0.0484

[a] Exact complex eigenmodes.

[b] Iterative complex eigenmodes.

[c] Approached complex eigenmodes (ACM), present work.

Table 5
Natural damped frequencies (Hz) and modal loss factors for the structure Fig. 4 and viscoelastic law Eq. (23).

	ω_1	ω_2	ω_3	ω_4	ω_5	η_1	η_2	η_3	η_4	η_5
20 °C										
Pristine	63.2	319.8	827.32	1541.5	1040.15	0.270	0.20	0.172	0.095	0.0210
Damaged	39.33	244.3	681.8	1334	10 134	0.039	0.011	0.0054	0.0023	0.01
27 °C										
Pristine	64.31	322.40	833.83	1586.72	1042.99	0.144	0.272	0.30	0.291	0.0484
Damaged	38.8	242.7	680.2	1331.5	1038.8	0.0025	0.0015	0.009	0.007	0.0204

The results presented in Table 4 show that the ACM method is more accurate in estimating ω_n than the ICM method. On the other hand, the ICM method slightly outperforms the ACM method in estimating η_n. Overall, the authors found no significant difference in the estimation of modal parameters between the two methods. However, we note that the computational cost of the ACM method is lower than that of the ICM method.

4. Delamination implementation in CUF 1D model

For simulating the delamination in FEM, region-based and layer-wise approaches are commonly used [49]. Since delamination modeling is complex and requires accurate kinematic fields, the CUF formulation allows various choices to describe the displacement fields precisely. In an LW model, simulating delamination may entail including an embedded layer at the interface [50–52]. It represents the delaminated zone as an artificially separated layer embedded within the structure. The constrained mode delamination model can be developed by reducing the stiffness properties of the embedded layer. The cross-section can be discretized, and each layer can be modeled using the LE (see Fig. 1(2)).

As the study's main objective is to exclusively investigate the VE damping mechanism in the delaminated structures, the influence of other damping mechanisms (contact and friction) is excluded. The mesh in the delaminated part is refined, meaning more LEs are used in the debonded zone. This refinement allows a more accurate representation of the delaminated region and its influence on the dynamic behavior of the structure.

Additionally, the thickness of the debonded layer is chosen to be as thin as possible. In Fig. 7, the embedded layer, whose thickness is a quarter of the thickness of the VE layer (0.01 of the total thickness of the beam in the whole interface) of the beam in Fig. 4 can be seen. Table 5 presents the effects of damage on the modal parameters of the structure for the first four bending modes and the first torsion mode.

In 4.1 and 4.2, the authors investigated the impact of symmetric and asymmetric delamination distributions on the modal parameters of the structure of Fig. 4. The objective was to comprehend how different delamination patterns affect the structural response. The embedded layer, representing the delaminated region, is positioned at the interface between the VE core and the elastic face. A high-mesh density is considered in the VE core, as shown in Fig. 8(2), to accurately capture the behavior of the delaminated zone. The CUF-based FE model used in the study allowed for a thin debonded zone, and contact effects were considered negligible. To gain further insights into the effects of BCs, the authors examined beams with three different BC configurations: clamped–free (CF), simply-supported (SS), and free–free (FF). The mode shapes considered in the analysis can be observed in Fig. 9.

4.1. Symmetrical delamination

Fig. 10(1) shows the first stage of damage introduced to the model (referred to as "damaged (a)"). Then, Three patterns of symmetrical delamination were studied.

1. Through-the-width symmetric delamination, see Fig. 10(2) (referred to as "damaged (b)").
2. Through-the-thickness symmetric delamination, see Fig. 14(2) (referred to as "damaged (c)").

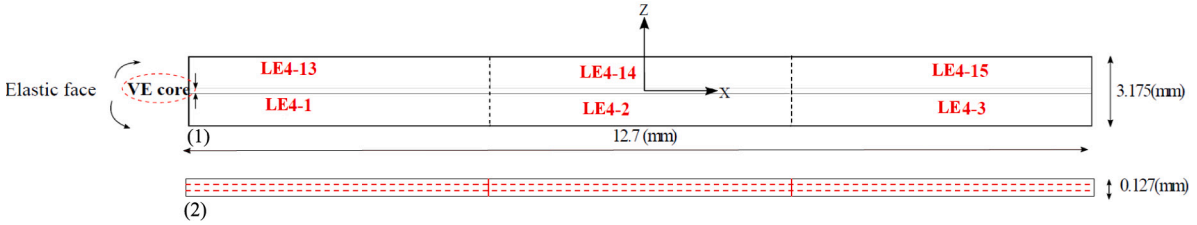

Fig. 8. (1) cross-section dimensions and mesh details and (2) VE core mesh refinement.

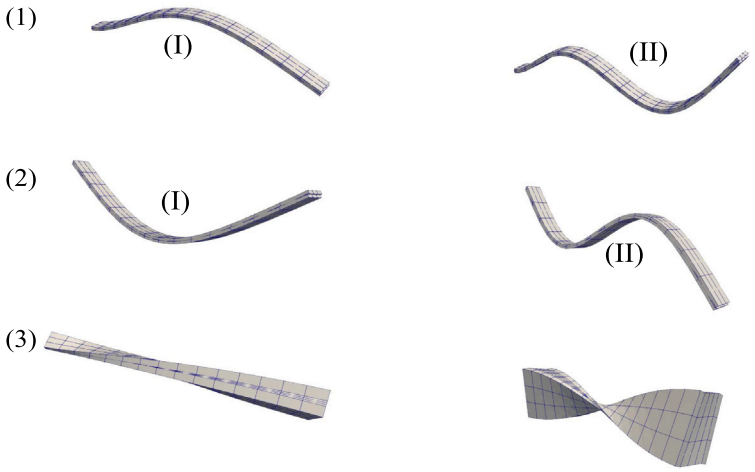

Fig. 9. (1) CF bending modes, (2) SS and FF bending modes (3) CF and FF torsion modes.

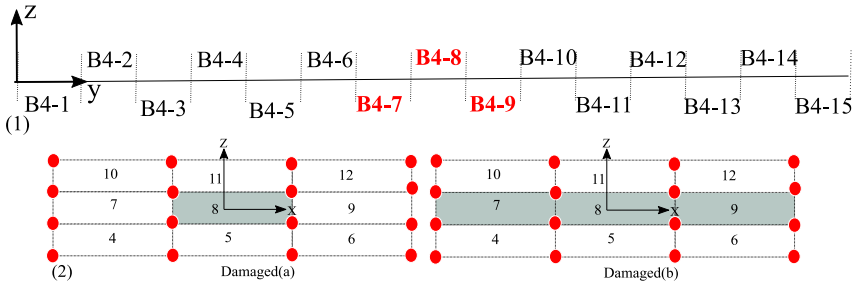

Fig. 10. (1) Debonded elements along the length in the red. (2) Symmetrical distribution of debonding along-the-width of the VE layer. (For interpretation of the references to color in this figure legend, the reader is referred to the web version of this article.)

3. Through-the-length symmetric delamination, see Fig. 18(2) (referred to as "damaged (d)").

In Figs. 10(1), 14(1) and 18(1)–(2), the debonded longitudinal elements are highlighted in color to indicate the delaminated regions. It is worth noting that the delamination size will not grow during the analysis (there is no defect propagation). Symmetric delamination patterns have been predetermined and compared with the initial damage state.

Through-the-width symmetric delamination

The authors introduced dimensionless modal parameters, namely $H = \frac{\eta_{\text{damaged}}}{\eta_{\text{pristine}}}$ and $\Omega = \frac{\omega_{\text{damaged}}}{\omega_{\text{pristine}}}$, to facilitate a comparison of the variations in modal parameters between pristine and damaged structures. These parameters allow for a quantitative assessment of the changes in modal characteristics. Fig. 10 depicts the delaminated zone within the structure. Figs. 11–12–13 present the variations in H and Ω for bending and torsional modes (as depicted in Fig. 9), respectively. These figures provide insights into how the modal parameters change due to the through-the-width delamination change in size.

Based on the results presented in Figs. 11–13, a transverse increase of the delamination size reduces the modal loss factors compared to the pristine structure. In bending modes, mode (II) variations are more intense than mode (I), which can be attributed to the difference in mode shapes. More significant changes in both torsion and bending modes can be observed in CF BCs. According to Fig. 13, torsional modes capture the symmetric transverse distribution of delamination well, especially for FF BCs. It suggests that torsional modes may be more sensitive to the symmetric distribution of delamination along the width of the structure.

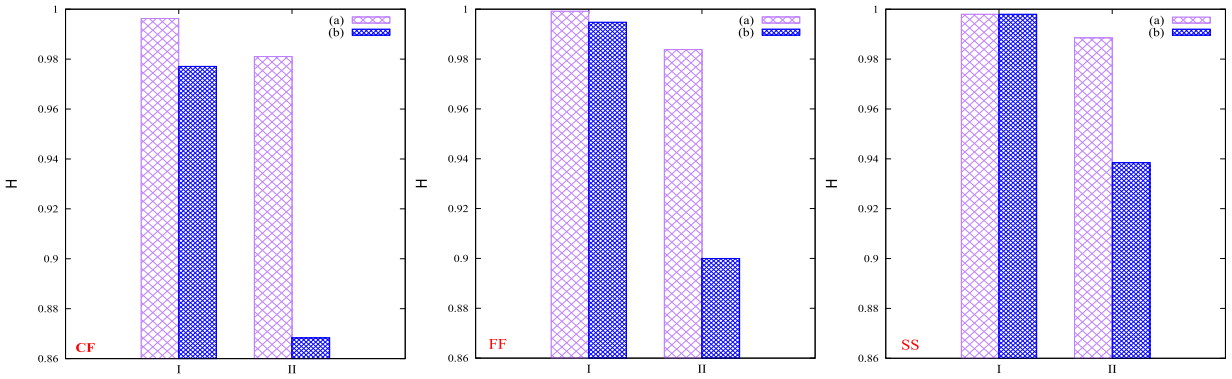

Fig. 11. Variations of the dimensionless modal loss factor relative to along-the-width symmetric size increment of debonding for CF, FF, and SS boundary conditions in bending modes.

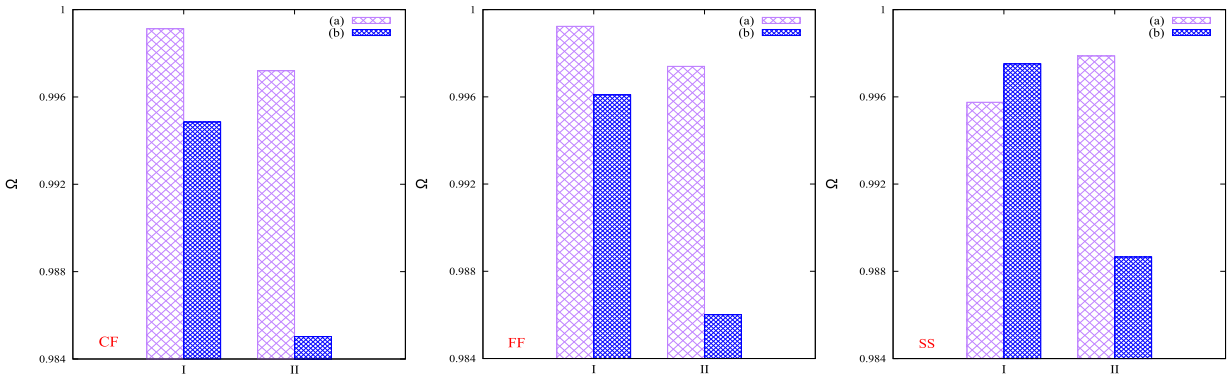

Fig. 12. Variations of the dimensionless natural frequency relative to along-the-width symmetric size increment of debonding for CF, FF, and SS boundary conditions in bending modes.

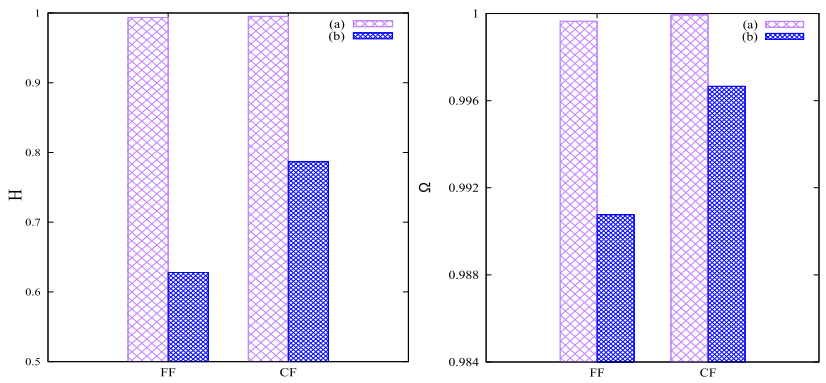

Fig. 13. Variations of the dimensionless modal loss factor and natural frequency relative to along-the-width symmetric size increment of debonding for CF and FF boundary conditions in torsion modes.

Through-the-thickness symmetric delamination

In this section, we study the symmetric, through-the-thickness debonding pattern. Figure 14(1), shows the debonded elements along-the-length and in the VE layer.

Fig. 15 depicts that in bending modes, the modal damping decreases with the expansion of delamination for mode (I) and increases for mode (II).

Figs. 15–17 show that bending modes are more sensitive to through-the-thickness delamination than torsional modes, even in a very small thickness.

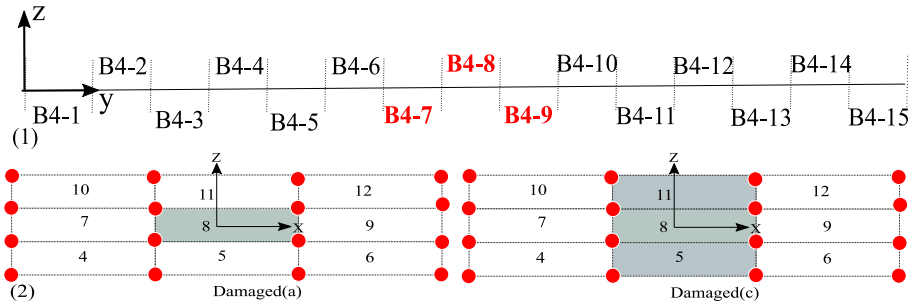

Fig. 14. (1) Debonded elements along-the-length in the red. (2) Symmetrical distribution of debonding along-the-thickness of the VE layer. (For interpretation of the references to color in this figure legend, the reader is referred to the web version of this article.)

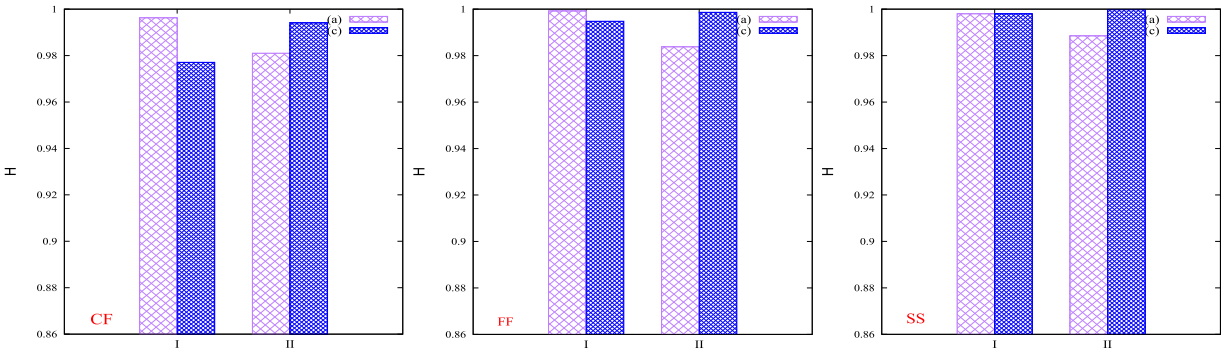

Fig. 15. Variations of the dimensionless modal loss factor relative to through-the-thickness size increment of debonding for CF, FF, and SS boundary conditions in modal bending modes.

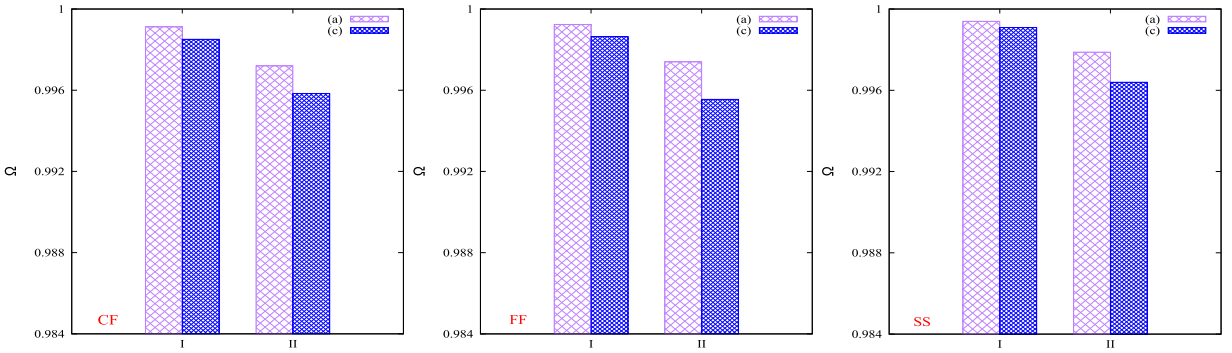

Fig. 16. Variations of the dimensionless natural frequency relative to through-the-thickness size increment of debonding for CF, FF, and SS boundary conditions in modal bending modes.

Through-the-length symmetric delamination

In Fig. 18, the distribution of the separated elements through-the-length and within the VE core are shown. The variations of H and Ω toward the longitudinal damage are found in Figs. 19–20–21 related to the bending and torsional mode shapes.

Fig. 19 provides significant insight in to the effect of symmetrical through-the-length delamination on H: for about 10% size variation in the longitudinal delamination, H correspondence to bending mode (II) varies more and up to 5%. This indicates a high sensitivity of bending modes to longitudinal delamination. However, torsional modes are less sensitive than bending modes in detecting through-the-length delamination, as shown in Fig. 21.

With the symmetrical size variation of delamination in width, thickness, and length directions, the sharpest H changes were observed in the CF BC, and the least changes were observed in SS. Figs. 22–23 compare the percentage of variations in the modal parameters of the damaged and pristine structures for the bending and torsion modes.

Based on Fig. 22, negative values were recorded in the current research for H variations in the bending modes. In contrast, both positive and negative values were observed in previous experimental research of the authors [6]. The authors believe that the

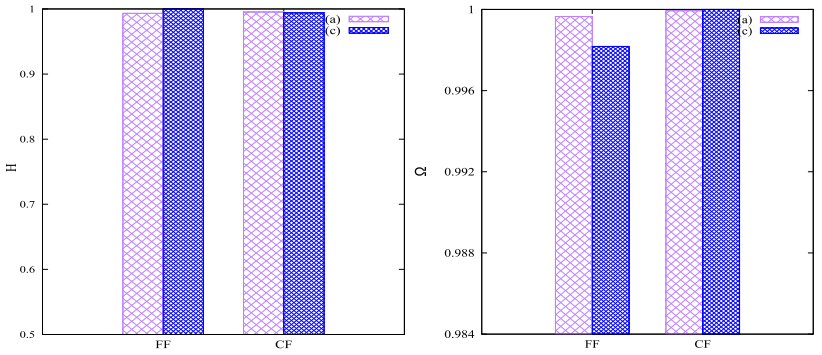

Fig. 17. Variations of the dimensionless modal loss factor and natural frequency relative to through-the-thickness symmetric size increment of debonding for CF and FF boundary conditions in modal torsion modes.

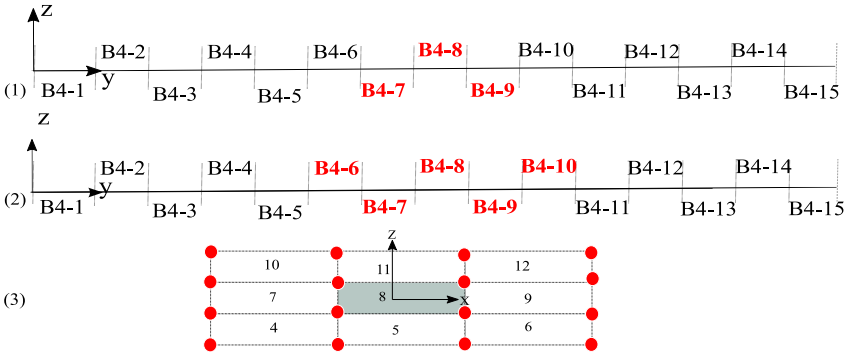

Fig. 18. (1) longitudinal schematics of damage (a) and (2) damage (d) and (3) debonded cross-sectional element in the VE core. (For interpretation of the references to color in this figure legend, the reader is referred to the web version of this article.)

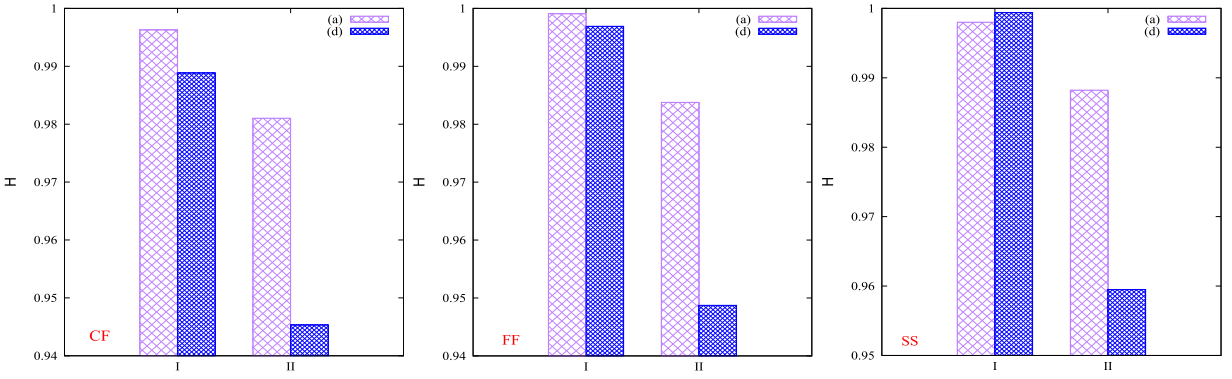

Fig. 19. Variations of the dimensionless modal damping relative to through-the-length size increment of debonding for CF, FF, and SS boundary conditions in modal bending modes.

positive values in the last study were probably due to the friction resulting from fiber breakage and highlight the complexity of the damping mechanisms in composite structures. Figs. 22–23 indicate that with damage expansion, the highest and lowest percentage variations in H and Ω are related to the transverse and longitudinal delamination change in size, respectively.

4.2. Comparison of symmetric and asymmetric delaminated beams

In this section, the effects of symmetric and asymmetric distribution of delamination on the modal behavior of the structure are compared. This comparison is crucial for understanding the effects of different delamination patterns on the structure's modal behavior. The choice of FF BCs for the beam is appropriate as it is geometrically symmetric. Fig. 24 illustrates the conversion of symmetric to asymmetric debonding distribution.

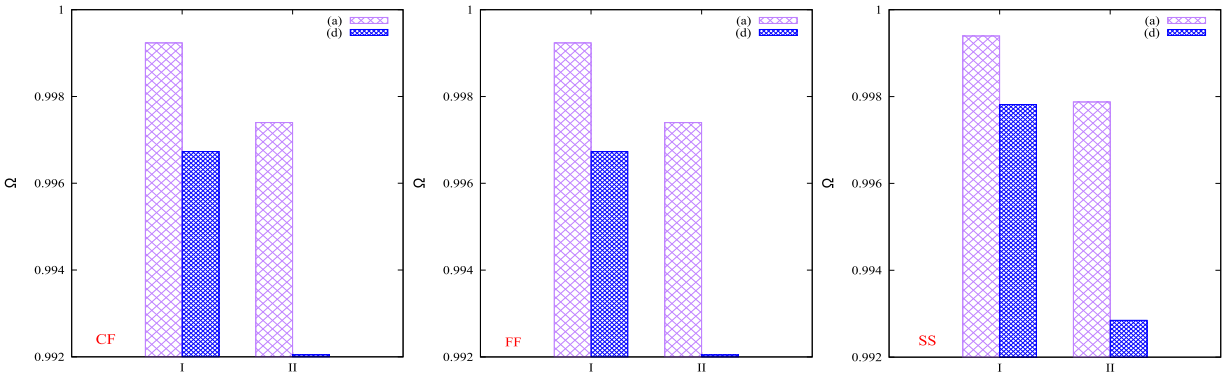

Fig. 20. Variations of the dimensionless natural frequency relative to through-the-length size increment of debonding for CF, FF, and SS boundary conditions in modal bending modes.

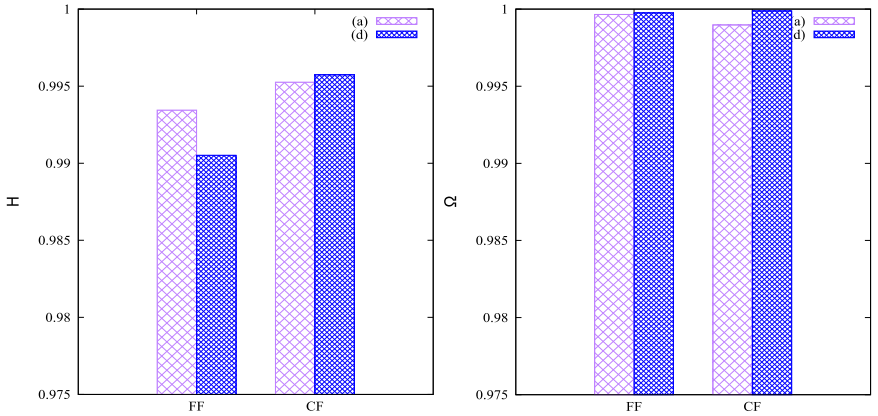

Fig. 21. Variations of the dimensionless modal loss factor and natural frequency relative to through-the-length size increment of debonding for CF and FF boundary conditions in modal torsion modes.

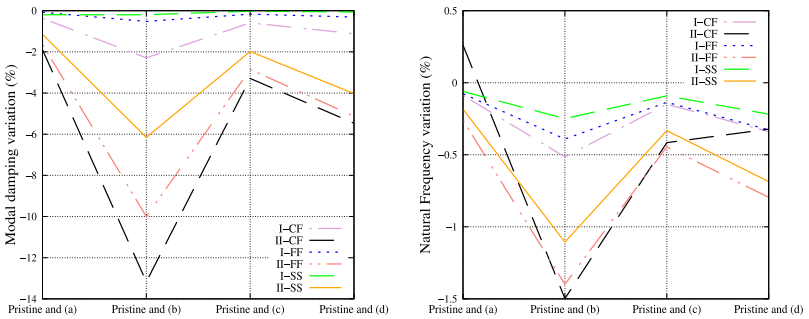

Fig. 22. Comparison of percentage changes of modal parameters of damaged and pristine for CF, FF, and SS boundary conditions in modal bending modes.

The comparison of the percentage of variations in mode (I) and mode (II) in Figs. 25–26 indicate that the percentage of variations in mode (I) is more than in mode (II) when switching from symmetric to asymmetric status. In the torsion mode, Fig. 26 shows that modal damping changes up to 8 percent for asymmetric distribution compared to symmetric one. This is an important finding as it suggests that torsional modes may be more sensitive to asymmetric delamination patterns than symmetric ones.

4.3. Boundary condition effect

In this part, the delamination in the CF beam around the extreme regions of displacement and strain is studied to understand the sensitivity of these parameters to delamination. The distribution of delamination in the cross-section is as Fig. 10(2). Fig. 28 represents the variations in beam modal parameters. As Fig. 28 indicates, the most and the least variations in H and Ω are in the

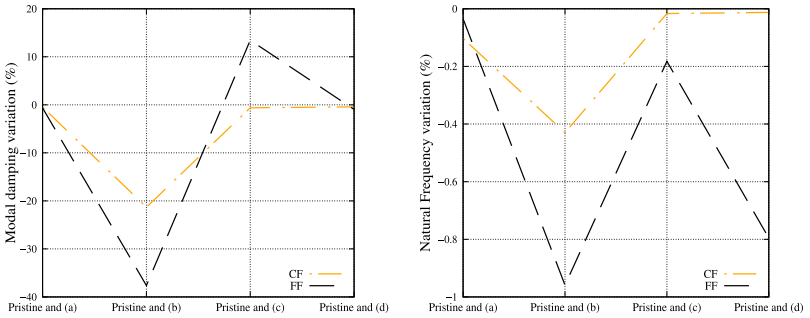

Fig. 23. Comparison of percentage of changes of modal parameters of damaged and pristine for CF and FF boundary conditions in modal torsion mode.

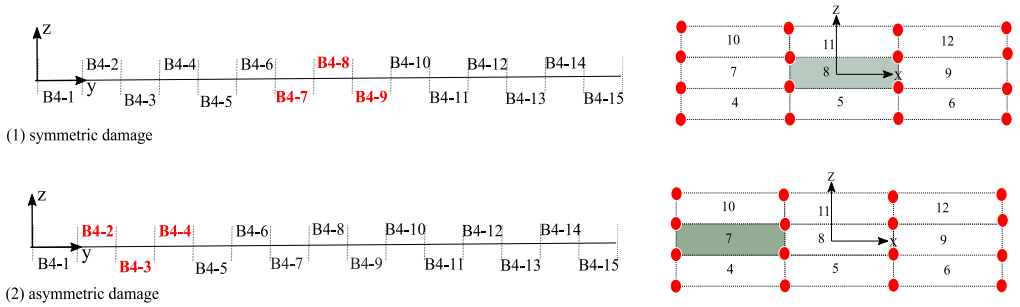

Fig. 24. Debonded elements through-the-length and in the cross-section in color in (1) symmetric and (2) asymmetric separation. (For interpretation of the references to color in this figure legend, the reader is referred to the web version of this article.)

region where the strain is maximum and minimum, respectively. Therefore, for the bending modes it is more likely to detect the damage if they are located in the maximum strain zone of the structure (see Fig. 27).

5. Conclusion

This research has focused on implementing layer-wise structural theories for parametric and complex eigenvalue analysis in 1D CUF-based models. The primary objective of this study is to detect the location and expansion of inter-laminar delamination by observing variations in global modal parameters. To verify the time domain estimation of the eigen parameters and modal damping, the circle fit method (CFM), an experimental modal analysis (EMA) technique, is used for frequency domain-based modal damping extraction. The reason for using CFM is that, among all EMA techniques, CFM yields the most accurate account of modal damping. The results of circle fit analysis were compared with the direct calculation of the modal damping from eigen parameters of the viscoelastic structure. The comparison revealed that EMA was successful in extracting the modal parameters. Additionally, the application of direct time-domain calculation of the FRF using the Prony series equivalent of E and η was compared to the direct frequency-domain eigensolution. The results showed a 5 to 10 percent difference in natural frequencies and a 10 to 30 percent difference in modal damping. As modal loss factor variations are much more visibly correlated with the delamination size variation than those of natural frequency, they are a more suitable parameter to use as a damage index. This finding is consistent with the authors' previous experimental research.

Furthermore, modal damping varies with the delamination location, with more significant variations observed around the maximum strain zone for bending modes and around the maximum deformation area for torsion modes.

In summary, this research provides valuable insights into using layer-wise structural theories for detecting inter-laminar delamination in VE structures. The study highlights the importance of modal parameters, particularly the modal loss factor, in detecting delamination size and location. The findings of this study can help develop non-destructive testing techniques for detecting inter-laminar delamination in VE structures.

Future work

In future work, the authors plan to model the effect of friction that arises from the contact between two oscillating damaged surfaces. Friction damping is believed to be one of the primary dissipation mechanisms in a delaminated structure, and its inclusion in the numerical model could provide additional insights into the damping behavior of the structure.

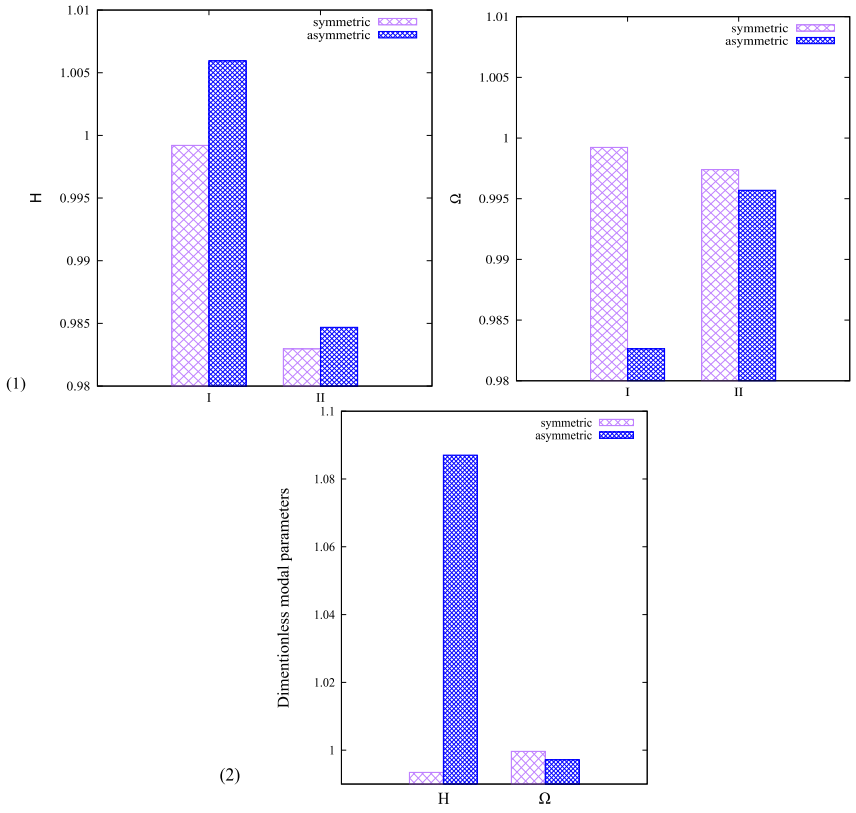

Fig. 25. Comparison of variation of modal parameters for symmetric and asymmetric damage dispensations for (1) modal bending modes and (2) modal torsion modes.

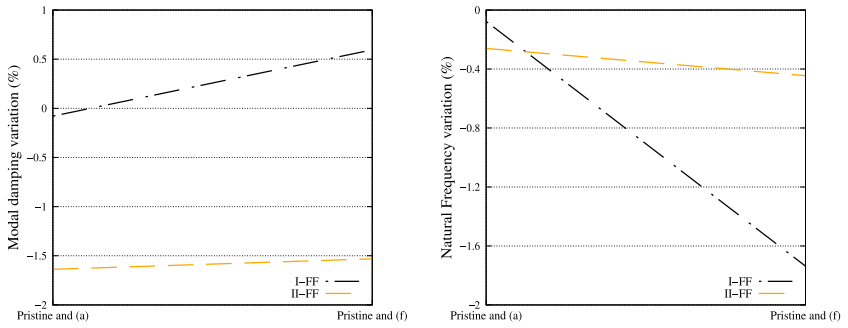

Fig. 26. Comparison of percentage changes of modal parameters for symmetric and asymmetric separations.

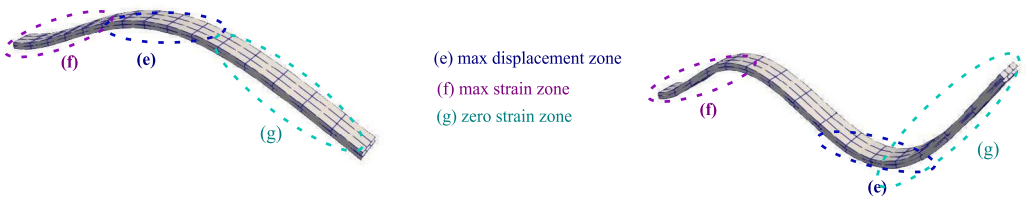

Fig. 27. Embedding delamination in different zones of the beam is shown in Fig. 4 for modes I and II.

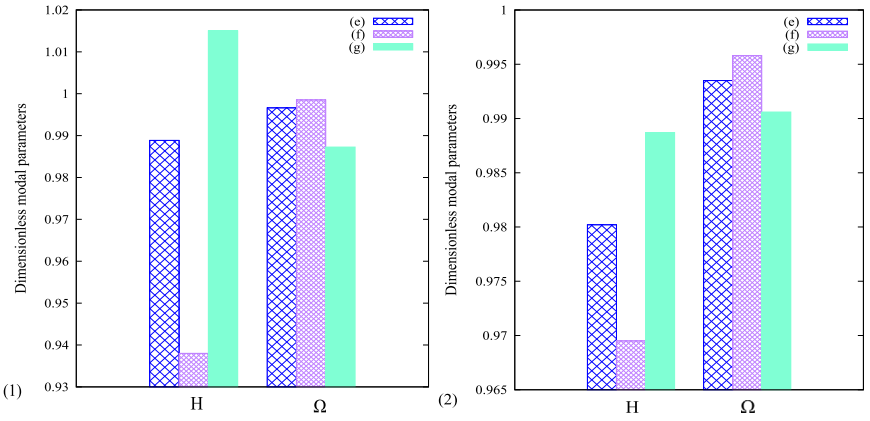

Fig. 28. The effect location of delamination on the modal parameter variations of CF beam (1) Mod I (2) Mod II.

CRediT authorship contribution statement

Sh. Kiasat: Writing – review & editing, Writing – original draft, Validation, Resources, Investigation, Formal analysis, Data curation. **A.S. Nobari:** Writing – review & editing, Supervision, Methodology. **M. Filippi:** Writing – review & editing, Supervision, Methodology. **E. Carrera:** Writing – review & editing, Supervision, Methodology.

Declaration of competing interest

The authors declare that they have no known competing financial interests or personal relationships that could have appeared to influence the work reported in this paper.

Data availability

Data will be made available on request.

References

[1] Y. Zou, L. Tong, G. Steven, Vibration-based model-dependent delamination identification and health monitoring for compos. struct.—a review, J. Sound Vib. 230 (2) (2000) 357–378.
[2] G. Hearn, R.B. Testa, Modal analysis for damage detection in structures, J. Struct. Eng. 117 (10) (1991) 3042–3063.
[3] S. Alampalli, Effects of testing, analysis, damage, and environment on modal parameters, Mech. Syst. Signal Process. 14 (11) (2000) 63–74.
[4] B. Shi, Z. Wang, H. Jing, Baseline-free delamination identification for composite cantilever beams based on high-order modal parameters in approximate waveform capacity dimension, J. Vib. Acoust. 141 (6) (2019).
[5] S.S. Naidu, C. Ratnam, Delamination identification of FRP composites usingg normalized modal curvature, Int. J. Mech. Product. Eng. Res. Dev. (IJMPERD) 10 (2020) 645–656.
[6] M. Khazaee, A.S. Nobari, M.H.F. Aliabadi, Experimental investigation of delamination effects on modal damping of a CFRP laminate, using a statistical rationalization approach, Vibration-Based Techniques for Damage Detection and Localization in Engineering Structures, World Scientific, 2018.
[7] A. Paolozzi, I. Peroni, Identification of models of a composite plate for the purpose of damage detection, Aerotec. Missili Spazio. 67 (1) (1988) 119–129.
[8] A. Paolozzi, I. Peroni, Detection of debonding damage in a composite plate through natural frequency variations, J. Reinf. Plast. Compos. 9 (4) (1990) 369–389.
[9] A.K. Pandey, M. Biswas, M.M. Samman, Damage detection from changes in curvature modeshapes, J. Sound Vib. 145 (2) (1991) 321–332.
[10] P. Qiao, K. Lu, W. Lestari, J. Wang, Curvature ModeShape-based damage detection in composite laminated plates, Compos. Struct. 80 (3) (2007) 409–428.
[11] B. Nanda, D. Maity, D.K. Maiti, Vibration based structural damage detection technique using particle swarm optimization with incremental swarm size, Int. J. Aeronaut. Space Sci. 13 (3) (2012) 323–331.
[12] T.R. Jebieshia, D. Maiti, D. Maity, Vibration characteristics and damage detection of compos. struct. with anisotropic damage using unified particle swarm optimization technique, in: Proceedings of the American Society for Composites, 13th Technical Conference, Michigan State University, East Lansing, MI, 2015, pp. 28–30.
[13] R. Chandra, S.P. Singh, K.L. Gupta, Damping studies in fiber-reinforced composites–a review, Compos. Struct. 46 (1) (1999) 41–51.
[14] X. Tang, X. Yan, A review on the damping properties of fiber reinforced polymer composites, J. Ind. Text. 49 (6) (2020) 693–721.
[15] D. Saravanos, D. Hopkins, Effects of delaminations on the damped dynamic characteristics of composite laminates: Analysis and experiments, J. Sound Vib. 192 (5) (1996) 977–993.
[16] L. Liu, Z. Bo-Ming, W. Dian-Fu, Z. Wu, Effects of cure cycles on void content and mechanical properties of composite laminates, Compos. Struct. 73 (3) (2006) 303–309.
[17] E. Benvenuti, O. Vitarelli, A. Tralli, Delamination of FRP-reinforced concrete by means of an extended finite element formulation, Composites B 43 (2012) 3258–3269.
[18] S. Hühne, J. Reinoso, E. Jansen, R. Rolfes, A two-way loose coupling procedure for investigating the buckling and damage behaviour of stiffened composite panels, Compos. Struct. 136 (2016) 513–525.
[19] O. Allix, P. Ladevèze, Interlaminar interface modelling for the prediction of delamination, Compos. Struct. 22 (4) (1992) 235–242.

[20] S.A. Ramu, V.T. Johnson, Damage assessment of compos. struct.—a fuzzy logic integrated neural network approach, Comput. Struct. 57 (3) (1995) 491–502.
[21] S. Hanagud, Delaminations in smart compos. struct.-a parametric study on vibrations, in: 31st Structures, Structural Dynamics and Materials Conference, 1990, pp. 28–30.
[22] A.S. Nobari, M.H.F. Aliabadi, Vibration-based techniques for damage detection and localization in engineering structures, vol. 10, World Scientific.
[23] K. Park, G.H. Paulino, Cohesive zone models: A critical review of traction-separation relationships across fracture surfaces, Appl. Mech. Rev. 64 (6) (2011) 060802.
[24] S. Zare Hosseinabadi, M.H. Sabour, M. Fakoor, Mixed-mode I/II criterion based on combining Hill failure analysis and reinforcement isotropic solid model, Acta Mech. 234 (4) (2023) 1437–1450.
[25] E. Carrera, A. Pagani, M. Petrolo, Classical, refined, and component-wise analysis of reinforced-shell wing structures, AIAA J. 51 (5) (2013) 1255–1268.
[26] E. Carrera, A. Pagani, M. Petrolo, Component-wise method applied to vibration of wing structures, J. Appl. Mech. 80 (4) (2013).
[27] E. Carrera, M. Maiarú, M. Petrolo, Component-wise analysis of laminated anisotropic composites, Int. J. Solids Struct. 49 (13) (2012) 1839–1851.
[28] E. Carrera, M. Petrolo, Refined beam elements with only displacement variables and plate/shell capabilities, Meccanica 47 (2012) 537–556.
[29] M. Petrolo, Advances in Predictive Models and Methodologies for Numerically Efficient Linear and Nonlinear Analysis of Composites, Springer, 2019.
[30] E. Carrera, M. Cinefra, M. Petrolo, E. Zappino, Finite Element Analysis of Structures Through Unified Formulation, John Wiley & Sons, 2014.
[31] K. Bathe, Finite element procedures, 1995.
[32] E. Carrera, M. Filippi, Variable Kinematic One-Dimensional Finite Elements for the Analysis of Rotors Made of Composite Materials J. Eng. Gas Turb. Power (136) (2014) 9.
[33] B. Ma, J. He, A finite element analysis of viscoelastically damped sandwich plates, J. Sound Vib. 152 (1) (1992) 107–9123.
[34] E. Ungar, Kerwin Jr., M. Edward, Loss factors of viscoelastic systems in terms of energy concepts, J. Acoust. Soc. Am. 34 (7) (1962) 954–957.
[35] M. Soni, Finite element analysis of viscoelastically damped sandwich structures, Shock Vib. Inform. Center Shock Vib. 55 (1) (1981) 97–109.
[36] H. Voss, An Arnoldi method for nonlinear eigenvalue problems, BIT Num. Math. 44 (3) (2004) 387–401.
[37] X. Chen, H. Chen, X. Hu, Damping prediction of sandwich structures by order-reduction-iteration approach, J. Sound Vib. 222 (5) (1999) 803–812.
[38] L. Duigou, M. Potier-Ferry, et al., Iterative algorithms for non-linear eigenvalue problems. Application to vibrations of viscoelastic shells, Comput. Methods Appl. Mech. Engrg. 192 (11–12) (2003) 1323–1335.
[39] M. Bilasse, E.M. Daya, L. Azrar, Linear and nonlinear vibrations analysis of viscoelastic sandwich beams, J. Sound Vib. 329 (23) (2010) 4950–4969.
[40] E. Barkanov, Method of complex eigenvalues for studying the damping properties of sandwich-type structures, Mech. Compos. Mater. 29 (1) (1993) 90–94.
[41] S. Kiasat, M. Filippi, A. Nobari, E. Carrera, Layer-wise dynamic analysis of a beam with global and local viscoelastic contributions using an FE/Laplace transform approach, Acta Mech. 223 (11) (2022) 4747–4761.
[42] E. Barkanov, E. Skukis, B. Petitjean, Characterisation of viscoelastic layers in sandwich panels via an inverse technique, J. Sound Vib. 327 (3–5) (2009) 402–412.
[43] M.A. Trindade, A. Benjeddou, R. Ohayon, Modeling of frequency-dependent viscoelastic materials for active-passive vibration damping, J. Vib. Acoust. 122 (2000) 169–174.
[44] M. Filippi, E. Carrera, A.M. Regalli, Layerwise analyses of compact and thin-walled beams made of viscoelastic materials, J. Vib. Acoust. 138 (6) (2016).
[45] M. Enelund, G.A. Lesieutre, Time domain modeling of damping using anelastic displacement fields and fractional calculus, Int. J. Solids Struct. 36 (29) (1999) 4447–4472.
[46] G.A. Lesieutre, U. Lee, A finite element for beams having segmented active constrained layers with frequency-dependent viscoelastics, Smart Mater. Struct. 5 (5) 615–627.
[47] M.A. Trindade, A. Marcelo, Reduced-order finite element models of viscoelastically damped beams through internal variables projection, J. Vib. Acoust. 128 (4) (2006) 501–508.
[48] D. Ewins, Modal Testing: Theory and Practice, Research Studies Press, 2009.
[49] C.N. Della, D. Shu, Vibration of delaminated composite laminates: A review, Appl. Mech. Rev. 60 (1) (2007) 1–20.
[50] R.B. Bharati, M. Filippi, P.K. Mahato, E. Carrera, Flutter analysis of delaminated composite box-beam using higher-order kinematics, Composites B 43 (2012) 3258–3269.
[51] E. Benvenuti, O. Vitarelli, A. Tralli, Delamination of FRP-reinforced concrete by means of an extended finite element formulation, Compos. Struct. 301 (2022) 116–145.
[52] Z. Zhou, A. Leung, X. Xu, The finite element discretized symplectic method for interface cracks, Composites B 58 (2014) 335–342.